5836 *Chem. Mater.* **2009,** *21,* 5836–5847
DOI:10.1021/cm902466p

CHEMISTRY OF MATERIALS
Article

Structural Investigation of Activated Lattice Oxygen in $Ce_{1-x}Sn_xO_2$ and $Ce_{1-x-y}Sn_xPd_yO_{2-\delta}$ by EXAFS and DFT calculation

Asha Gupta,[†] M. S. Hegde,*[,‡] K. R. Priolkar,[§] U. V. Waghmare,[∥] P. R. Sarode,[§] and S. Emura[⊥]

[†]*Materials Research Centre,* [‡]*Solid State and Structural Chemistry Unit, Indian Institute of Science, Bangalore 560012, India,* [§]*Department of Physics, Goa University, Taleigao Plateau, Goa 403206, India,* [∥]*Theoretical Sciences Unit, Jawaharlal Nehru Centre for Advanced Scientific Research, Jakkur Campus, Bangalore 560064, India, and* [⊥]*Institute of Scientific and Industrial Research, Osaka University, Mihoga-oka 8-1, Ibaraki, Osaka, 567-0047, Japan*

Received August 11, 2009. Revised Manuscript Received October 27, 2009

Substitution of Sn^{4+} ion in CeO_2 creates activated oxygen in $Ce_{0.8}Sn_{0.2}O_2$ leading to higher oxygen storage capacity compared to $Ce_{0.8}Zr_{0.2}O_2$. With Pd ion substitution in $Ce_{0.8}Sn_{0.2}O_2$, activation of oxygen is further enhanced as observed from the H_2/TPR study. Both EXAFS analysis and DFT calculation reveal that in the solid solution Ce exhibits 4 + 4 coordination, Sn exhibits 4 + 2 + 2 coordination and Pd has 4 + 3 coordination. While the oxygen in the first four coordination with short M−O bonds are strongly held in the lattice, the oxygens in the second and higher coordinations with long M−O bonds are weakly bound, and they are the activated oxygen in the lattice. Bond valence analysis shows that oxygen with valencies as low as 1.65 are created by the Sn and Pd ion substitution. Another interesting observation is that H_2/TPR experiment of $Ce_{1-x}Sn_xO_2$ shows a broad peak starting from 200 to 500 °C, while the same reduction is achieved in a single step at ∼110 °C in presence Pd^{2+} ion. Substitution of Pd^{2+} ion thus facilitates synergistic reduction of the catalyst at lower temperature. We have shown that simultaneous reduction of the Ce^{4+} and Sn^{4+} ions by Pd^0 is the synergistic interaction leading to high oxygen storage capacity at low temperature.

1. Introduction

Release of oxygen from CeO_2 fluorite lattice for CO oxidation in autoexhaust and its reversible uptake of oxygen from stream is defined as the oxygen storage capacity (OSC):[1,2] $CeO_2 + \delta CO \rightarrow CeO_{2-\delta} + \delta CO_2$, $CeO_{2-\delta} + {}^{\delta}/_{2}O_2 \rightarrow CeO_2$. Quantitatively, δ is the OSC. Thus, CeO_2 is continuously reduced and oxidized following the well-known Mars-van Krevelen mechanism. Application of oxygen storage materials in autoexhaust catalysis has led to the development of CeO_2-based oxygen storage materials, prominent among them being $Ce_{1-x}Zr_xO_2$.[3−6] Substitution of Zr in CeO_2 not only increases the OSC, the temperature at which oxygen is extracted by CO was lowered compared to CeO_2, even though ZrO_2 itself is not a reducible oxide. Higher reducibility and CO oxidation activity of $Ce_{1-x}Zr_xO_2$ at lower temperature indicates that the lattice oxygen is more activated compared to CeO_2. Solid solutions of TiO_2 and SnO_2 with CeO_2 of the type $Ce_{1-x}Ti_xO_2$ and $Ce_{1-x}Sn_xO_2$ have been reported from this laboratory to show high OSC and low temperature activity, and the concept of activation of lattice oxygen has been invoked.[7−9] On the basis of DFT calculations, Metiu and co-workers have reported that dopant atom weakens the surrounding oxygen bond of the doped oxide making it a better oxidant and thus facilitates CO oxidation.[10,11] Incorporation of noble metal ions like Pd^{2+} and Pt^{2+} in CeO_2 and $Ce_{1-x}M_xO_2$ (M = Zr, Ti, and Sn) is reported to further enhance the OSC and catalytic activity of the catalyst.[7,8,12−15] In addition to application in the catalytic converters to minimize the emission of toxic pollutants (CO, NO_x, and hydrocarbons, etc.) from automobile exhaust, these high oxygen storage materials have

*Corresponding author. E-mail: mshegde@sscu.iisc.ernet.in.

(1) Gandhi, H. S.; Graham, G. W.; McCabe, R. W. *J. Catal.* **2003**, *216*, 433.
(2) Yao, H. C.; Yao, Y. F. Y. *J. Catal.* **1984**, *86*, 254.
(3) Ozawa, M.; Kimura, M.; Isogai, A. *J. Alloys Compd.* **1993**, *193*, 73.
(4) Nagai, Y.; Yamamoto, T.; Tanaka, T.; Yoshida, S.; Nonaka, T.; Okamoto, T.; Suda, A.; Sugiura, M. *Catal. Today* **2002**, *74*, 225.
(5) Fornasiero, P.; Dimonte, R.; Rao, G. R.; Kaspar, J.; Meriani, S.; Trovarelli, A.; Graziani, M. *J. Catal.* **1995**, *151*, 168.
(6) Baidya, T.; Hegde, M. S.; Gopalakrishnan, J. *J. Phys. Chem. B* **2007**, *111*, 5149.
(7) Baidya, T.; Gayen, A.; Hegde, M. S.; Ravishankar, N.; Dupont, L. *J. Phys. Chem. B* **2006**, *110*, 5262.
(8) Baidya, T.; Gupta, A.; Deshpandey, P. A.; Madras, G.; Hegde, M. S. *J. Phys. Chem. C* **2009**, *113*, 4059.
(9) Baidya, T.; Dutta, G.; Hegde, M. S.; Waghmare, U. V. *Dalton Trans.* **2009**, 455.
(10) Nolan, M.; Verdugo, V. S.; Metiu, H. *Surf. Sci.* **2008**, *602*, 2734.
(11) Shapovalov, V.; Metiu, H. *J. Catal.* **2007**, *245*, 205.
(12) Hegde, M. S.; Madras, G.; Patil, K. C. *Acc. Chem. Res.* **2009**, *42*, 704.
(13) Baidya, T.; Marimuthu, A.; Hegde, M. S.; Ravishankar, N.; Madras, G. *J. Phys. Chem. C* **2007**, *111*, 830.
(14) Bekyarova, E.; Fornasiero, P.; Kaspar, J.; Graziani, M. *Catal. Today* **1998**, *45*, 179.
(15) Roy, S.; Marimuthu, A.; Hegde, M. S.; Madras, G. *Appl. Catal., B* **2007**, *71*, 23.

 Published on Web 11/30/2009

potential applications in generation of hydrogen fuel via water−gas shift reaction[16,17] and thermo chemical splitting of water,[18] partial oxidation of methane to produce syngas[19] and oxidation of methanol[20] and formaldehyde.[21,22] In order to find new high oxygen storage materials of the type $Ce_{1-x}Zr_xO_2$, it is essential to understand the mechanism behind improved OSC, and hence the process by which activation of lattice oxygen occurs in these CeO_2-based fluorite lattices.

According to Trovarelli[23] any chemical modification of CeO_2 involving an increase in the number of defects (oxygen vacancies) should produce a material with higher oxygen storage capacity. Numerous studies have been carried out to understand the enhanced reducibility based on physical and structural properties and first principle calculations by many groups.[4,23−29] Nagai et al. have studied local structure of Zr and Ce in CeO_2-ZrO_2 with different homogeneity of the samples, and showed that different homogeneity results in different coordination number (CN) around Zr ion, whereas the CN of Ce was reported to be 8 in all samples.[4] According to Vlaic et al. Zr ion is too small to accommodate eight oxygen atoms in its first coordination sphere, favoring a displacement of one oxygen atom at a nonbonding distance from Zr ion; this order/disorder oxygen sublattice generated by Zr ion in CeO_2 enhances the reducibility of the mixed oxides.[26] Earlier studies based on EXAFS and first principle calculations from this laboratory, have shown that higher reducibility of CeO_2-ZrO_2 and CeO_2-TiO_2 solid solutions is the result of distortion of oxygen sublattice creating long and short Ce−O and Zr−O/Ti−O bonds, and the longer bonds can be utilized for CO oxidation.[27,30]

Recently 2% Pd ion substituted CeO_2-SnO_2 solid solution was reported to show much higher OSC and catalytic activity because of the highly labile lattice oxygen and oxide ion vacancies compared to CeO_2-ZrO_2 solid solution.[8] Unlike Zr which can adopt only +4 oxidation, Sn can adopt two oxidation states: Sn^{2+} and Sn^{4+}. This Sn^{4+}/Sn^{2+} redox couple can also participate in redox reactions along with Ce^{4+}/Ce^{3+} couple. The local coordination around Sn^{4+} ion should be different from that of an ideal fluorite CeO_2 structure because Sn^{4+} is a smaller ion (Shannon ionic radii, $r = 0.81$ Å) compared to Ce^{4+} ion ($r = 0.97$ Å). SnO_2 crystallizes in rutile structure and CN of Sn is 6 which is different from 8-fold coordination of Ce in CeO_2. These differences in the structure open the possibility of substantial perturbation within the ceria lattice. Thus, the questions that arise and should be addressed are as follows: (a) How the local coordination of dopant Sn ion and the host Ce ion changes on substitution in the fluorite? (b) If the concentration of the dopant Sn is increased, does it further increase the stress in the host lattice? (c) How smaller percentage of Pd ion substitution in the solid solution changes the oxygen sublattice around Ce, Sn, and Pd? (d) Can we relate M−O bond distances (M = Pd, Sn, Ce) with OSC and tell how the destabilization of the oxygen bonds can lead to higher reducibility of the solid solution? To probe into such issues, we carried out H_2/TPR studies of $Ce_{1-x}Sn_xO_2$ and $Ce_{1-x-y}Sn_xPd_yO_{2-\delta}$ ($x = 0.2$ and 0.5, $y = 0.02$) systems complemented with first-principles DFT calculations. The theoretically determined structures have been compared with the local structure obtained from EXAFS analysis. We show that the local coordination of Ce, Sn and Pd gets modified into long and short bonds from the ideal 8-fold coordination present in fluorite lattice. The longer oxygen bonds are weakly held in the lattice and these oxygen act as activated oxygen. We propose that simultaneous reduction of the Ce^{4+} and Sn^{4+} ions by the reduced Pd^0 is the synergistic interaction responsible for high OSC at lower temperature.

2. Methods

2.1. Experiment. $Ce_{1-x}Sn_xO_2$ ($x = 0.1-0.5$) was prepared by the solution combustion method using ceric ammonium nitrate, tin oxalate, and glycine. For the preparation of $Ce_{0.5}Sn_{0.5}O_2$, 5.48 g (0.01 mol) of $(NH_4)_2Ce(NO_3)_6$ (Loba Chemie, 99%), 2.07 g (0.01 mol) of SnC_2O_4 (precipitated from $SnCl_2$, Sigma Aldrich, 99.9%), and 3.67 g (0.049 mol) of glycine ($C_2H_5O_2N$, Merck, 99%) were taken, and dissolved in minimum volume of HNO_3 and 20 mL of water in a 300 mL crystallizing dish to form a clear solution. The dish was then kept in a preheated furnace at 320 °C. The combustion started after dehydration, and the product was obtained within 60 s. For synthesizing $Ce_{0.8}Zr_{0.2}O_2$, $(NH_4)_2Ce(NO_3)_6$, $Zr(NO_3)_4 \cdot 5H_2O$ (Loba Chemie, 99%), and glycine were taken in molar ratio 0.8:0.2:2.58. For 2 atom % Pd ion substituted $Ce_{0.8}Sn_{0.2}O_2/Ce_{0.8}Zr_{0.2}O_2$, $(NH_4)_2Ce(NO_3)_6$, $PdCl_2$ (Sigma Aldrich, 99.9+%), $SnC_2O_4/Zr(NO_3)_4$, and L-tartaric acid (Laboratory Rasayan, 97%)/glycine were taken in 0.78:0.02:0.2:2.42/2.52 molar ratio.

XRD data were recorded on a Philips X'Pert diffractometer at a scan rate of 0.12°/min with a 0.02° step size in the 2θ range between 20° and 100°. X-ray photoelectron spectra were recorded on a Thermo Fisher Scientific Multilab 2000 (England) instrument with Al Kα radiation (1486.6 eV). The binding energies reported here is with reference to graphite at 284.5 eV

(16) Fu, Q.; Weber, A.; Flytzani-Stephanopoulos, M. *Catal. Lett*. **2001**, *77*, 87.
(17) Hilaire, S.; Wang, X.; Luo, T.; Gorte, R. J.; Wagner, J. *Appl. Catal., A* **2004**, *258*, 271.
(18) Abanades, S.; Flamant, G. *Solar Energy* **2006**, *80*, 1611.
(19) Pino, L.; Recupero, V.; Beninati, S.; Shukla, A. K.; Hegde, M. S.; Bera, P. *Appl. Catal., A* **2002**, *225*, 63.
(20) Scibioh, M. A.; Kim, S.-K.; Cho, E. A.; Lim, T.-H.; Hong, S.-A.; Ha, H. Y. *Appl. Catal., B* **2008**, *84*, 773.
(21) Shen, Y.; Yang, X.; Wang, Y.; Zhang, Y.; Zhu, H.; Gao, L.; Jia, M. *Appl. Catal., B* **2008**, *79*, 142.
(22) Tang, X.; Chen, J.; Huang, X.; Xu, Y.; Shen, W. *Appl. Catal., B* **2008**, *81*, 115.
(23) Trovarelli, A. *Catalysis by Ceria and Related Materials*; Imperial College Press: London, U.K., 2002.
(24) Shah, P. R.; Kim, T.; Zhou, G.; Fornasiero, P.; Gorte, R. J. *Chem. Mater*. **2006**, *18*, 5363.
(25) Lemaux, S.; Bensaddik, A.; van der Eerden, A. M. J.; Bitter, J. H.; Koningsberger, D. C. *J. Phys. Chem. B* **2001**, *105*, 4810.
(26) Vlaic, G.; Fornasiero, P.; Geremia, S.; Kaspar, J.; Graziani, M. *J. Catal*. **1997**, *168*, 386.
(27) Dutta, G.; Waghmare, U.; Baidya, T.; Hegde, M.; Priolkar, K.; Sarode, P. *Catal. Lett*. **2006**, *108*, 165.
(28) Andersson, D. A.; Simak, S. I.; Skorodumova, N. V.; Abrikosov, I. A.; Johansson, B. *Appl. Phys. Lett*. **2007**, *90*, 031909.
(29) Andersson, D. A.; Simak, S. I.; Skorodumova, N. V.; Abrikosov, I. A.; Johansson, B. *Phys. Rev. B: Condens. Matter Mater. Phys*. **2007**, *76*, 174119.
(30) Dutta, G.; Waghmare, U. V.; Baidya, T.; Hegde, M. S.; Priolkar, K. R.; Sarode, P. R. *Chem. Mater*. **2006**, *18*, 3249.

or Ag ($3d_{5/2}$) at 368.2 eV having an accuracy of ± 0.1 eV. Oxide samples were ground with 30 wt % graphite powder, made into thin pellet at room temperature. For transmission electron microscopy (TEM) studies, an acetone dispersion of the sample was dropped onto holey carbon-coated Cu grids, and the images were recorded with FeI Technai 20 instrument at 200 kV. Temperature programmed reduction (TPR) was carried out by passing 5% H_2 in Ar at a 30 mL/min flow rate at heating rate of 10 °C/min over 50 mg of oxide, and the amount of H_2 uptake was detected by using a TCD detector, which was calibrated against the uptake of H_2 with a known amount of CuO. Reoxidation was carried out by passing pure oxygen at 300 °C, cooled to room temperature and the H_2 uptake experiment was then repeated with the reoxidized sample.

Ce L_3, Sn K, and Pd K edge EXAFS spectra in catalyst and reference samples were recorded at room temperature in the transmission mode with Si (111) double-crystal monochromators at BL0B1 beamline at SPring-8, Japan. The Ce EXAFS spectra were scanned in the range of 5.425−6.145 keV and the Sn EXAFS was scanned from 28.93 to 30.22 keV, while 24.01−25.30 keV formed the range of scan for Pd EXAFS spectra. The photon energy was calibrated for each scan with respect to Cu K and Pd K edge in respective metal foils. Both the incident (I_o) and transmitted (I) synchrotron beam intensities were measured simultaneously using ionization chamber filled with appropriate gases. The absorbers were made by pressing the fine powder samples into pellets of 10 mm diameter with boron nitride. To avoid the sample thickness effect, the edge step ($\Delta\mu_0$x) was restricted to a value ≤1 by adjusting the thickness of the absorber pellet where $\Delta\mu_0$ is edge step in the absorption coefficient and x is the sample thickness.[31] EXAFS data analysis was done using ATHENA and ARTEMIS program.[32] The value of amplitude reduction factor (S_o^2) is deduced from the EXAFS spectra of respective metals with known crystal structural data.[33] The theoretical calculation of back scattering amplitude and phase shift functions are obtained by using FEFF (6.01) program.[34] The experimental EXAFS data was fitted with the theoretical EXAFS function in ARTEMIS.

2.2. Theory. We use plane wave self-consistent field (PWscf)[35] implementation of DFT with periodic boundary conditions to relax the internal structure. Our total energy calculations are based on local density approximation (LDA) to the exchange correlation energy of electrons. Interaction between valence electrons and ionic cores is treated using first-principles ultrasoft pseudopotentials[36] and a plane wave basis with an energy cut off of 30 Ry in the representation of the Kohn−Sham wave functions was employed. Semicore states of Ce and Sn are included in the valence and spin polarization is not considered in our calculation. The total energy was minimized with respect to lattice constant for CeO_2 fluorite structure, whereas for the other system, the lattice parameter was kept constant at the values obtained from Rietveld refined XRD results, and only the internal atomic positions were relaxed to minimize the total energy. We have performed calculation for the following system:

(a) Pure CeO_2 was simulated in the fluorite structure with conventional cubic unit cell (with four formula units of CeO_2) integrals over the Brillouin zone were sampled on 6 × 6 × 6 Monkhorst−Pack[37] k-point mesh. The primitive unit cell has three atoms where Ce atom is located at (0, 0, 0) and the two oxygen atoms at (± 0.25, ± 0.25, ± 0.25).

(b) To simulate the doping of smaller percentage (~2 atom %) Pd ion in $Ce_{1-x}Sn_xO_2$, a larger unit cell is needed. We use a 2 × 2 × 2 supercell (built from conventional cubic cell) comprising 96 atoms (i.e., 32 formula units of CeO_2) for simulating $Ce_{0.5}Sn_{0.5}O_2$ system. 50% Sn substitution was done by randomly substituting 16 Ce atoms with Sn atoms, and the Brillouin zone integration was sampled on 4 × 4 × 4 k-point mesh.

(c) $Ce_{0.8}Sn_{0.2}O_2$ system was simulated using a similar 96-atom supercell model. Six Ce atoms were replaced by Sn, and the formula of the resultant cell is $Ce_{26}Sn_6O_{64}$ corresponding to 18.75% of Sn substitution in CeO_2, close to the experimental composition.

(d) For the 2% Pd ion substitution in $Ce_{1-x}Sn_xO_2$ solid solution, an additional Ce atom was replaced by Pd in the 2 × 2 × 2 supercell and one oxide ion vacancy was created to compensate for the charge created by lower valent Pd^{2+} substitution. The resulting formulas are represented as $Ce_{25}Sn_6Pd_1O_{63}$ and $Ce_{16}Sn_{15}Pd_1O_{63}$ corresponding to additional 3.125% Pd in the solid solution.

The M−O bond lengths (M = Ce, Sn Pd) determined from the optimized structures are used to estimate bond valence of oxygen following the bond valence method described by Brown and O'Keeffe.[38] Bond valence is defined as (a) $s_i = \exp[-(R_i - R_0)/B]$ for Ce−O and Pd−O bond and (b) $s_i = (R_i/R_0)^{-N}$ for Sn−O, where R_i is the ith bond length, R_0 is the length of a bond of unit valence, and B and N are the fitted parameters. The atomic valence V is obtained by summing the bond valencies associated with a particular ion given by $V = \Sigma_i s_i$.

3. Results and Discussion

Characterization of the samples was done with XRD to check whether palladium ions are substituted into $Ce_{1-x}Sn_xO_2$ matrix. XRD patterns of as-prepared $Ce_{1-x}Sn_xO_2$ and 2 atom % Pd substituted oxide, shown in Figure 1a and b, were identical and could be indexed to the standard CeO_2 with fluorite structure (JCPDS no. 340394) and diffraction lines due tin-oxide or palladium-oxide were not observed indicating formation of solid solution given by the formula $Ce_{0.8}Sn_{0.2}O_2$ and $Ce_{0.5}Sn_{0.48}Pd_{0.02}O_{2-\delta}$, respectively. The XRD patterns of $Ce_{0.78}Sn_{0.2}Pd_{0.02}O_{2-\delta}$ and $Ce_{0.5}Sn_{0.5}O_2$ were refined by the Rietveld method using the Fullprof Suite Program.[39] Refinement was carried out by simultaneously varying 18 parameters that include the overall scale factor, background parameters, unit cell, half width, shape, and isotropic thermal parameters along with the oxygen

(31) Stern, E. A.; Kim, K. *Phys. Rev. B* **1981**, *23*, 3781.
(32) Ravel, B.; Newville, M. *J. Synchrotron Rad.* **2005**, *12*, 537.
(33) Pearson, W. P. *Handbook of Lattice Spacing and Structure of Metals and Alloys*; Pergamon: New York, 1958.
(34) Zabinsky, S. I.; Rehr, J. J.; Ankudinov, A.; Albers, R. C.; Eller, M. J. *Phys. Rev. B* **1995**, *52*, 2995.
(35) Baroni, S.; Dal Corso, A.; de Gironcoli, S.; Giannozzi, P.; Cavazzoni, C.; Ballabio, G.; Scandolo, S.; Chiarotti, G.; Focher, P.; Pasquarello, A.; Laasonen, K.; Trave, A.; Car, R.; Marzari, N.; Kokalj, A. http://www.pwscf.org/.
(36) Vanderbilt, D. *Phys. Rev. B: Condens. Matter Mater. Phys.* **1990**, *41*, 7892.
(37) Monkhorst, H. J.; Pack, J. D. *Phys. Rev. B* **1976**, *13*, 5188.
(38) Brown, I. D. The Bond-Valence Method: An Empirical Approach to Chemical Structure and Bonding. In *Structure and Bonding in Crystals*; O'Keeffe, M., Navrotsky, A., Eds.; Academic Press: New York, 1981; Vol. *2*.
(39) Rodriguez-Carvajal, J. Multi-pattern Rietveld Refinement Program Fullprof. 2k, version 3.30; Laboratiore Léon Brillouin, CEA: Saclay, France, June 2005-LLB.

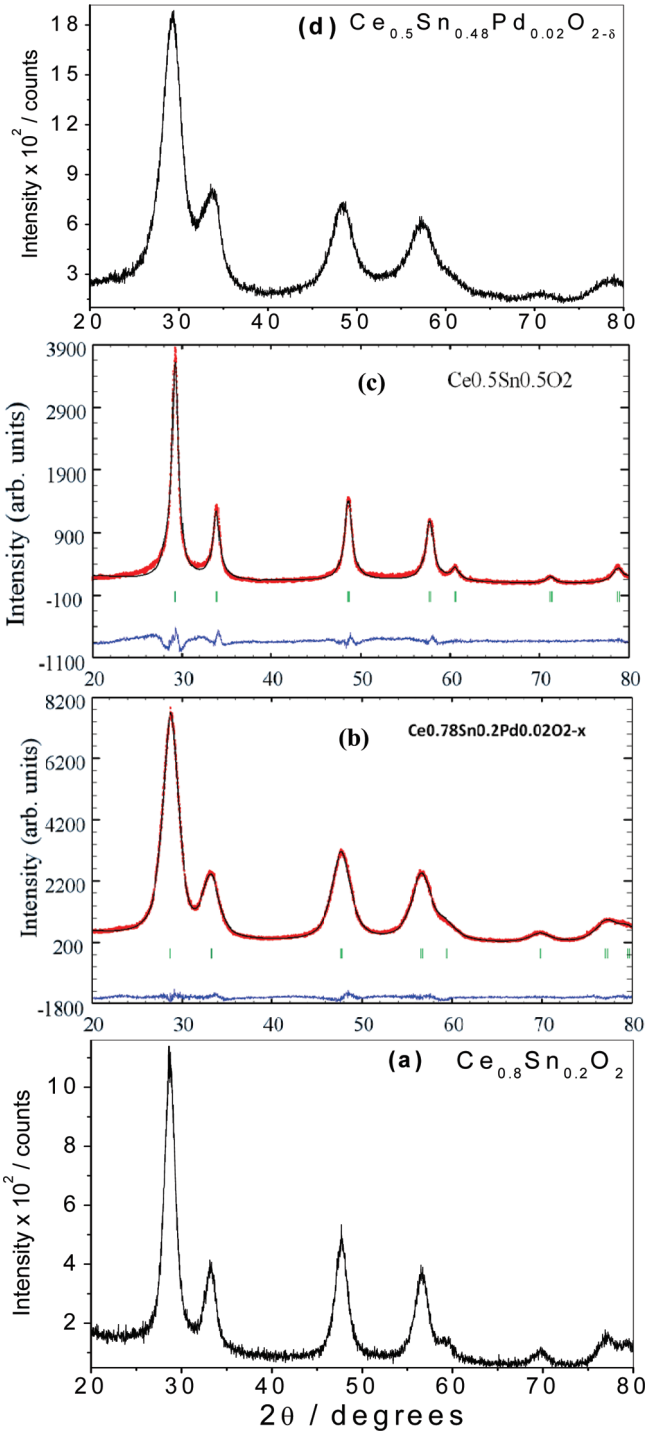

Figure 1. (a) XRD pattern of $Ce_{0.8}Sn_{0.2}O_2$. Rietveld refined XRD pattern of (b) $Ce_{0.78}Sn_{0.2}Pd_{0.02}O_{1.98}$ and (c) $Ce_{0.5}Sn_{0.5}O_2$. (d) XRD of $Ce_{0.5}Sn_{0.48}Pd_{0.02}O_{1.98}$.

occupancy; Sn^{4+} and Pd^{2+} ions were taken in Ce^{4+} sites. The typical observed XRD patterns along with the calculated pattern are shown in panels b and c of Figure 1. The goodness of the profile refinements were determined from the *R* values, given in Table 1. Decrease in lattice parameter is observed with the increase in Sn substitution which is consistent with the substitution of smaller Sn^{4+} (ionic radii, $r = 0.81$ Å) ion for larger Ce^{4+} ($r = 0.97$ Å) ion; on Pd^{2+} ion ($r = 0.86$ Å) substitution the lattice parameter further decreases.

Table 1. Rietveld Refined Lattice Parameters of $Ce_{0.8}Sn_{0.2}O_2$, $Ce_{0.78}Sn_{0.2}Pd_{0.02}O_{1.98}$, $Ce_{0.5}Sn_{0.5}O_2$, and $Ce_{0.5}Sn_{0.48}Pd_{0.02}O_{1.98}$

catalyst	lattice parameter, *a* (Å)	R_{Bragg}	R_f	χ^2
CeO_2 (JCPDS No. 340394)	5.411			
$Ce_{0.8}Sn_{0.2}O_2$	5.3948(5)	0.92	0.77	1.01
$Ce_{0.78}Sn_{0.2}Pd_{0.02}O_{1.98}$	5.3893(7)	0.40	0.34	1.49
$Ce_{0.5}Sn_{0.5}O_2$	5.2931(1)	2.49	1.58	3.01
$Ce_{0.5}Sn_{0.48}Pd_{0.02}O_{1.98}$	5.2861(2)	2.35	1.25	3.22

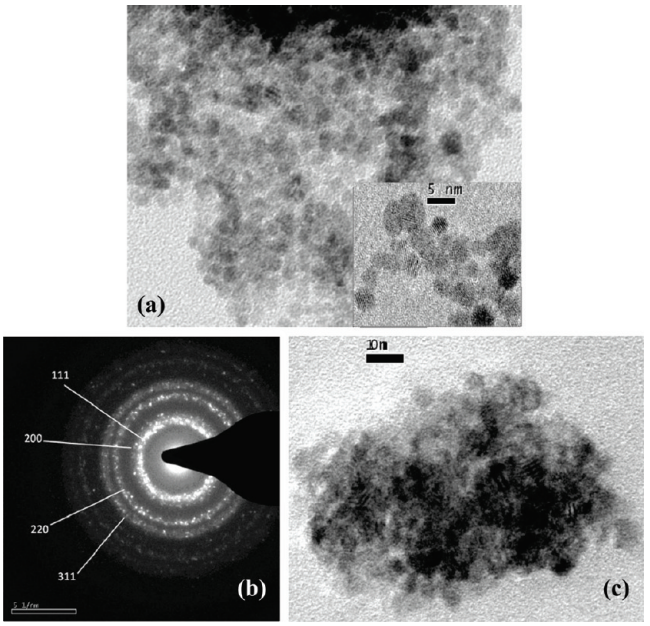

Figure 2. (a) Bright field TEM image of $Ce_{0.78}Sn_{0.2}Pd_{0.02}O_{1.98}$, the high resolution-TEM (inset) and (b) the indexed diffraction pattern, and the (c) bright field TEM image of $Ce_{0.5}Sn_{0.48}Pd_{0.02}O_{1.98}$.

Transmission electron microscope image of $Ce_{0.78}Sn_{0.2}Pd_{0.02}O_{2-\delta}$ and $Ce_{0.5}Sn_{0.5}O_2$ are shown in Figure 2. The bright field image of $Ce_{0.78}Sn_{0.2}Pd_{0.02}O_{2-\delta}$ is given in panel (a) and the crystallite sizes are in the range of 3−5 nm. The inset of Figure 2a shows the high resolution micrograph image; well-defined lattice fringes indicate that the particles are crystalline in nature and presence of other phase is not observed. Selected area diffraction pattern of $Ce_{0.78}Sn_{0.2}Pd_{0.02}O_{2-\delta}$ is shown in the panel b and it is indexed to fluorite structure and no other ring pattern is observed. The bright field image of $Ce_{0.5}Sn_{0.5}O_2$ is given in Figure 2c, the crystallite sizes are in the range of 5−8 nm.

The reactivity of lattice oxygen and oxygen storage/release property of oxide catalyst is measured by H_2/TPR; the values of OSC and composition of the reduced compound are summarized in Table 2. H_2-TPR profiles of $Ce_{0.8}Sn_{0.2}O_2$ and $Ce_{0.78}Sn_{0.2}Pd_{0.02}O_{1.98}$ are shown in Figure 3. In case of $Ce_{0.8}Sn_{0.2}O_2$, reduction starts from 200 °C, peak is observed at 300 °C and continues up to 550 °C. OSC corresponding to this broad reduction peak is ∼1700 μmol g^{-1} and the composition of the reduced catalyst is given as $Ce_{0.8}Sn_{0.2}O_{1.71}$. In case of $Ce_{0.78}Sn_{0.2}Pd_{0.02}O_{1.98}$, a sharp peak appears at 110 °C, OSC for the reduction up to 150 °C is 1650 μmloes. gm^{-1} and the composition of the reduced sample is $Ce_{0.78}Sn_{0.2}Pd_{0.02}O_{1.70}$. PdO itself is reduced by H_2 at ∼80 °C.[40]

(40) Paryjczak, T.; Farbotko, J. M.; Jóźwiak, K. W. *React. Kinet. Catal. Lett.* **1982**, *20*, 227.

Table 2. OSC Measured from H_2/TPR Experiment and the Composition of the Reduced Oxides

catalyst	OSC in μmol g^{-1}	composition of the reduced sample
CeO_2	180	$CeO_{1.97}$
$Ce_{0.8}Sn_{0.2}O_2$	1720	$Ce_{0.8}Sn_{0.2}O_{1.71}$
$Ce_{0.8}Zr_{0.2}O_2$	1130	$Ce_{0.8}Zr_{0.2}O_{1.81}$
$Ce_{0.78}Sn_{0.2}Pd_{0.02}O_{1.98}$	1650	$Ce_{0.78}Sn_{0.2}Pd_{0.02}O_{1.70}$
$Ce_{0.78}Zr_{0.2}Pd_{0.02}O_{1.98}$	620	$Ce_{0.78}Zr_{0.2}Pd_{0.02}O_{1.88}$
$Ce_{0.5}Sn_{0.5}O_2$	2600	$Ce_{0.5}Sn_{0.5}O_{1.58}$
$Ce_{0.5}Sn_{0.48}Pd_{0.02}O_{1.98}$	1330	$Ce_{0.5}Sn_{0.48}Pd_{0.02}O_{1.77}$

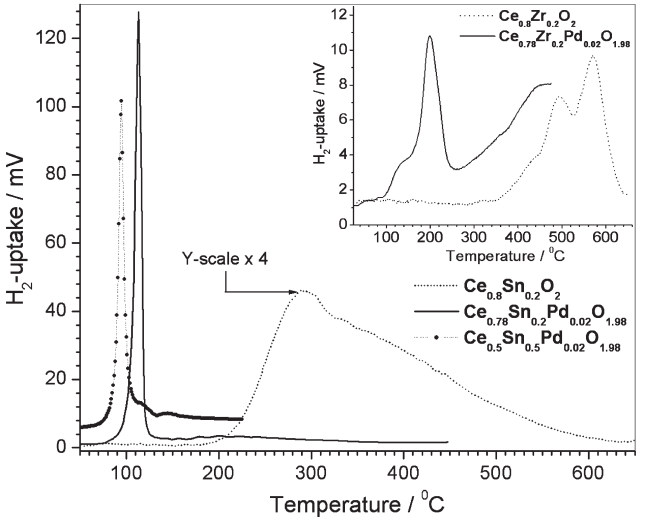

Figure 3. H_2/TPR profiles of $Ce_{0.8}Sn_{0.2}O_2$ (magnified 4 times), $Ce_{0.78}Sn_{0.2}Pd_{0.02}O_{1.98}$ and $Ce_{0.5}Sn_{0.48}Pd_{0.02}O_{1.98}$; the inset shows the H_2/TPR profiles of $Ce_{0.8}Zr_{0.2}O_2$ and $Ce_{0.78}Zr_{0.2}Pd_{0.02}O_{1.98}$.

So it is evident that the extent reduction for $Ce_{0.8}Sn_{0.2}O_2$ starting from 200 to 550 °C is achieved sharply at 110 °C because of Pd^{2+} ion substitution. Thus reduction temperature of Ce^{4+} and Sn^{4+} is brought down from ~300 °C for $Ce_{0.8}Sn_{0.2}O_{2-\delta}$ to 110 °C for $Ce_{0.78}Sn_{0.2}Pd_{0.02}O_{1.98}$, indicating enhanced activation of lattice oxygen in presence of Pd^{2+} ion.

Oxygen storage/release property of $Ce_{0.8}Zr_{0.2}O_2$ and $Ce_{0.78}Zr_{0.2}Pd_{0.02}O_{1.98}$ are given in the inset of Figure 3 for comparison. For $Ce_{0.8}Zr_{0.2}O_2$, the reduction starts from 400 °C and continues up to 600 °C which corresponds to OSC of 1130 μmol.gm^{-1}. With Pd^{2+} ion substitution hydrogen uptake peaks appears at ~ 200 °C and the total OSC up to 200 °C is 620 μmol.gm^{-1}. Here also we observe that in presence of Pd^{2+} ion hydrogen uptake peak is shifted to lower temperature, but the effect is less pronounced compared to $Ce_{0.78}Sn_{0.2}Pd_{0.02}O_{1.98}$ system.

To check the reversibility of hydrogen uptake property of $Ce_{0.78}Sn_{0.2}Pd_{0.02}O_{2-\delta}$ catalyst, the H_2/TPR cycles were carried out several times after oxidizing the reduced sample in O_2/air at 300 °C. Figure 4a shows fifteen TPR cycles with the same sample and the H_2 uptake peak at 110 °C is found to be reversible. The area under the peak up to 150 °C is used to estimate the oxygen storage capacity (OSC) of the catalyst. OSC of $Ce_{0.78}Sn_{0.2}Pd_{0.02}O_{2-\delta}$ measured for the all 15 cycles are given in Figure 4b. The H_2/Pd ratio is between 12 to14 indicating that H_2 uptake peak is reversible. The composition of the reduced catalyst from H_2/TPR analysis is given as

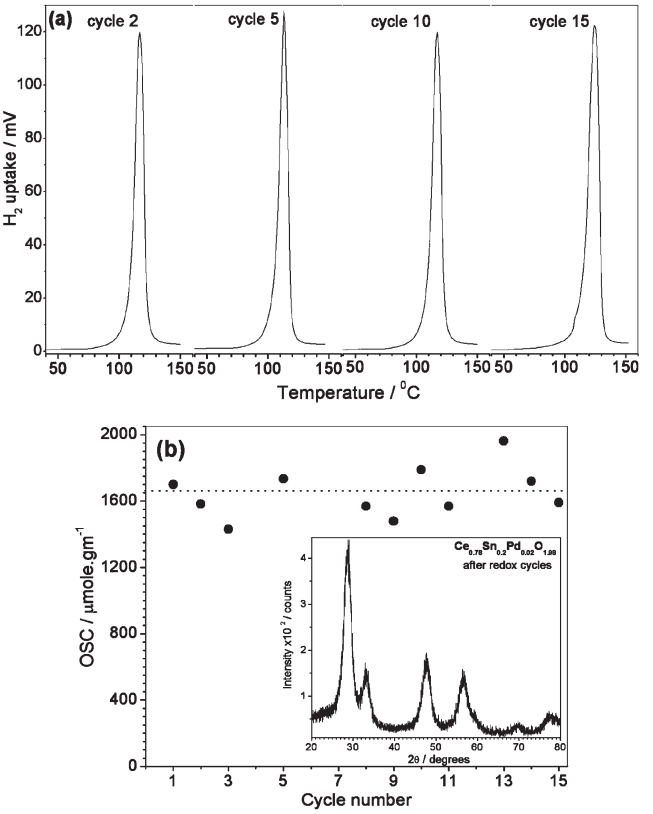

Figure 4. (a) Several H_2/TPR cycles of $Ce_{0.78}Sn_{0.2}Pd_{0.02}O_{1.98}$. (b) Plot of OSC vs H_2/TPR cycles and the XRD pattern after 15 cycles (inset).

$Ce_{0.78}Sn_{0.2}Pd_{0.02}O_{1.98-\delta}$, where $\delta = 0.23-0.29$ corresponding to OSC of 1450−1700 μmol gm^{-1}. XRD pattern of $Ce_{0.78}Sn_{0.2}Pd_{0.02}O_{2-\delta}$ after the redox cycles is shown in the inset of Figure 4b; no phase separation is observed indicating that fluorite structure is stable under several redox cycles.

To see the H_2 uptake behavior of the sample when oxygen vacancy are present in $Ce_{0.78}Sn_{0.2}Pd_{0.02}O_{1.98}$, the oxide was reduced to an intermediate temperature of 100 °C (before the peak reduction temperature is achieved), then it was cooled down to 0 °C under Ar-flow, followed by H_2-uptake cycle. Three cycles of partial reduction, followed by H_2/TPR run, were carried out, and the profiles are shown in Figure 5. There is a shift in the peak reduction temperature toward lower temperature of 45 °C, confirming the fact that oxygen sublattice gets further destabilized with the creation of oxygen vacancies leading to higher reactivity of the catalyst.

H_2/TPR studies of $Ce_{0.5}Sn_{0.5}O_2$ and $Ce_{0.5}Sn_{0.48}Pd_{0.02}O_{1.98}$ were also performed, and OSC measured for $Ce_{0.5}Sn_{0.5}O_2$ is 2600 μmol g^{-1} for reduction up to 550 °C, and for $Ce_{0.5}Sn_{0.48}Pd_{0.02}O_{1.98}$, it is 1330 μmol g^{-1} for reduction up to 150 °C. Though the OSC of $Ce_{0.5}Sn_{0.48}Pd_{0.02}O_{1.98}$ is smaller than that of $Ce_{0.78}Sn_{0.2}Pd_{0.02}O_{1.98}$, the peak reduction temperature of the former is shifted to lower temperature of 90 °C. Therefore, 2% Pd-substituted $Ce_{0.5}Sn_{0.5}O_2$ has a lower OSC compared to that of $Ce_{0.78}Sn_{0.2}Pd_{0.02}O_{1.98}$, but the oxygen is more reactive in the former.

EXAFS Studies. The Fourier transforms (FT) of k^3-weighted $\chi(k)$ for Ce L_3-edge EXAFS of $Ce_{0.8}Sn_{0.8}O_2$ and

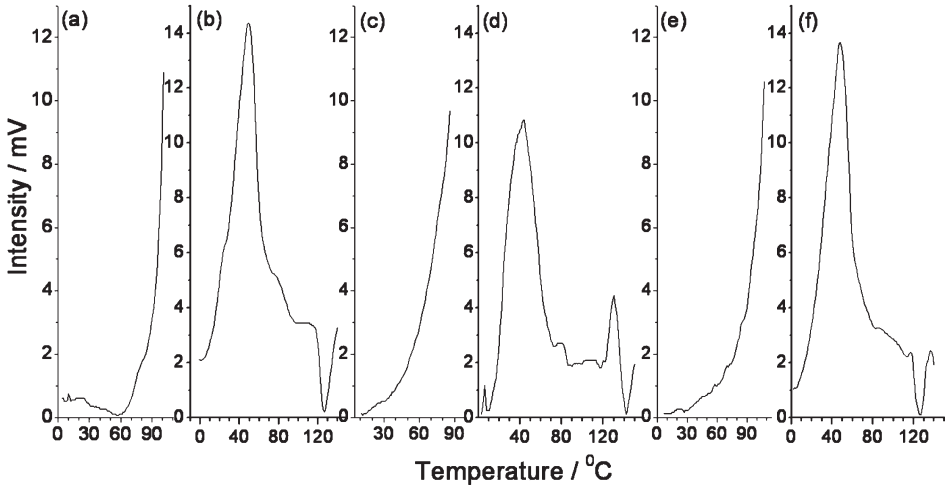

Figure 5. Three H_2/TPR of $Ce_{0.78}Sn_{0.2}Pd_{0.02}O_{1.98}$ for reduction up to 100 °C (panels a, c and e), followed by complete H_2/TPR run (panels b, d and f).

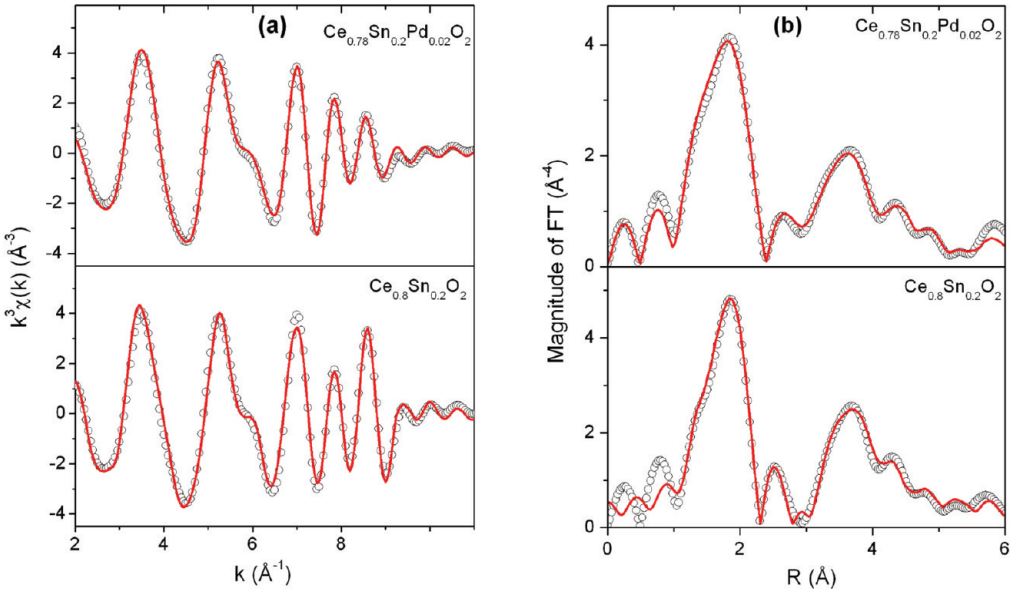

Figure 6. (a) The background subtracted Ce L_3-edge EXAFS of $Ce_{0.8}Sn_{0.8}O_2$ and $Ce_{0.78}Sn_{0.8}Pd_{0.02}O_{1.98}$ and (b) the corresponding backtransforms; the solid lines indicate fits to the data.

$Ce_{0.78}Sn_{0.8}Pd_{0.02}O_{2-\delta}$ are shown in Figure 6a. The weighted EXAFS data were transformed to *R* space and the resultant backtransformed data along with the fit are presented in Figure 6b. The radial distribution in Figure 6b are not phase corrected for phase shifts, so the observed peaks are shifted to lower *R* values from the true interatomic distances. The values of the bond lengths given in the text and in Tables 3 and 4 along with the Debye−Waller terms are phase corrected. In fluorite structure, Ce has 8 and 12 neighboring atoms in the first and second coordination shell corresponding to Ce−O and Ce−Ce correlations. But the EXAFS data could not be fitted with single Ce−O distance with 8 coordination for the first shell of neighboring atoms. Hence the magnitude of FT for Ce L_3-edge were fitted considering 4 + 4, 6 + 2 and 4 + 2 + 2 coordination of Ce and the best fitting with 4 + 4 coordination is shown in Figure 6. For $Ce_{0.8}Sn_{0.8}O_2$ the fitting gave phase corrected distances at 2.20 and 2.37 Å corresponding to Ce−O correlations; the longer distances at 3.45 and 3.68 Å are attributed to Ce−Sn and Ce−Ce correlations corresponding to coordination number of 2 and 10 respectively, which is approximately in the same Sn/Ce ratio as that of the sample. For $Ce_{0.78}Sn_{0.8}Pd_{0.02}O_{2-\delta}$, the good fit was obtained for 4 + 4 coordination, and the bond lengths at 2.20 and 2.41 Å in 4:4 ratio are assigned to Ce−O correlations and the longer distances at 3.45 and 3.72 Å are assigned to Ce−Sn and Ce−Ce correlations.

The background subtracted k^3-weighted Sn *K* EXAFS function with the fit and its inverse Fourier transformed magnitude along with the fit of $Ce_{0.8}Sn_{0.8}O_2$ and $Ce_{0.78}Sn_{0.8}Pd_{0.02}O_{2-\delta}$ samples are given in Figure 7. Since Sn^{4+} ion is smaller than Ce^{4+} ion, oxygen sub lattice around Sn^{4+} ion is distorted from ideal 8-fold coordination of fluorite structure. Hence fitting of oxygen coordination around Sn was done using 6 + 2, 4 + 4 and 4 + 2 + 2 coordination. The backtransformed *k* space of Sn *K*-edge was best fitted with 4 + 2 + 2 coordination;

Table 3. Local Coordination and Bond Length in $Ce_{0.8}Sn_{0.2}O_2$ from Ce L_3 and Sn *K*-edge EXAFS

Shell	coord. No.	*R* (Å)	σ^2 (Å^{-2})
	Ce L_3-EXAFS		
Ce−O(I)	4.0	2.20(1)	0.008(2)
Ce−O(II)	4.0	2.37(1)	0.006(1)
Ce−Sn	2.0(4)	3.45(2)	0.003(1)
Ce−Ce	10.0(5)	3.68(1)	0.003(1)
	Sn K-EXAFS (4 + 2 + 2)		
Sn−O(I)	4.3 (2)	2.03(3)	0.004(1)
Sn−O(II)	1.6(4)	2.20(1)	0.007(2)
Sn−O(III)	1.8(5)	2.43(3)	0.013(5)
	Sn K-EXAFS (6 + 2)		
Sn−O(I)	6.5(3)	2.03(6)	0.006(1)
Sn−O(II)	1.5(1)	2.63(4)	0.02
	Sn K-EXAFS (4 + 4)		
Sn−O(I)	4.1 (2)	1.99(4)	0.004(1)
Sn−O(II)	3.8(2)	2.24(1)	0.019(2)

and the resultant fitting for both $Ce_{0.8}Sn_{0.8}O_2$ and $Ce_{0.78}Sn_{0.8}Pd_{0.02}O_{2-\delta}$ is shown Figure 7a. The FT were fitted with 6 + 2, 4 + 4, and 4 + 2 + 2 distributions, and the resultant fitting is shown in Figure 7b; from the Debye−Waller terms, presented in Tables 3 and 4, the best fit among the three distributions was obtained for 4 + 2 + 2 coordination. For $Ce_{0.8}Sn_{0.8}O_2$ sample, the fitting gave coordination number as 4.3, 1.6, and 1.8 corresponding to distances of 2.03, 2.20, and 2.43 Å, respectively, which are the result of Sn−O correlations. The FT fitting for $Ce_{0.78}Sn_{0.8}Pd_{0.02}O_{2-\delta}$ gave same coordination number of 4 + 2 + 2 and same bond distances as that of $Ce_{0.8}Sn_{0.8}O_2$. The σ^2 values for 2.20 and 2.43 Å distances are comparatively higher than the 2.03 Å bond length indicating that the four Sn−O distances are somewhat distributed over the region of 2.2−2.5 Å.

The k^3-weighted Pd *K*-edge and its inverse FT of $Ce_{0.78}Sn_{0.8}Pd_{0.02}O_{2-\delta}$ are shown in Figure 8. The best fit gave 4 + 2 coordination around Pd at distances 2.02 and 2.52 Å respectively due to Pd−O correlations. The correlations observed at higher distances at 2.99, 3.39, and 3.54 Å are attributed to Pd−Pd, Pd−Ce, and Pd−Sn shell, respectively. Therefore, from the EXAFS data analysis, the Ce−O bond length are fitted with 4 + 4 coordination at ~2.2 and ~ 2.4 Å, respectively, while the ideal Ce−O bond distance is 2.34 Å in pure CeO_2. Thus substitution of Sn and Pd ion affects the 8-fold coordination around Ce ion. Sn exhibits 4 + 2 + 2 coordination while Pd has 4 + 2 coordination in the solid solution.

DFT Calculations. At minimum energy the optimized lattice parameter of CeO_2 is 5.42 Å, which is close to the experimental value of 5.411 Å (JCPDS No. 340394), with all Ce−O bond lengths equal to 2.34 Å (Figure 9a). For $Ce_{0.8}Sn_{0.2}O_2$, simulated with $Ce_{26}Sn_6O_{64}$ supercell (see optimized bond lengths in the form of a histogram in Figure 9b), we find that Sn substitution results in substantial distortion of the oxygen sublattice with longer and shorter Ce−O bonds compared to CeO_2. From some of the typical Ce−O bond lengths, summarized in Table 5, it is evident that Ce is essentially in 4 + 4 coordination. The Ce−O bonds are distributed over a range from short (2.16 Å) to long (2.64 Å) bonds with the mean short Ce−O bonds equal to 2.26(0.05) Å and long bonds equal to 2.45(0.12 Å). Out of 8 coordination of Sn, first 4 coordination are bunched at ~2.05 Å and the next 4 coordination are broadly distributed from 2.3 to 2.75 Å. Mean bond lengths, calculated assuming 4 + 2 + 2 coordination, are 2.03(0.3), 2.46(0.15) and 2.71(0.12) Å, respectively (see Table 6). The deviation of the mean distances for the first coordination shell is small and in the second and third coordination shell it is somewhat large.

Table 4. Local Coordination and Bond Length in $Ce_{0.8}Sn_{0.2}O_2$ from Ce L_3, Sn *K* and Pd *K*-edge EXAFS

shell	coord. no.	*R* (Å)	σ^2 (Å^{-2})
	Ce L_3 EXAFS		
Ce−O(I)	4.0	2.20(1)	0.008(2)
Ce−O(II)	4.0	2.41(1)	0.006(1)
Ce−Sn	2.0(4)	3.45(1)	0.003(1)
Ce−Ce	10.0(5)	3.72(2)	0.003(1)
	Sn K EXAFS		
Sn−O(I)	4.3 (2)	2.03(3)	0.004(1)
Sn−O(II)	1.6(4)	2.20(1)	0.007(2)
Sn−O(III)	1.8(5)	2.43(3)	0.013(5)
	Pd K EXAFS		
Pd−O(I)	4.4(2)	2.03(4)	0.007(1)
Pd−O(II)	2.0(3)	2.52(1)	0.005(1)
Pd−Pd	1.7(4)	2.99(2)	0.011(2)
Pd−Ce	3.4(10)	3.39(4)	0.027(7)
Pd−Sn	1.8(8)	3.54(5)	0.017(6)

From the optimized bond lengths of 2 atom % Pd doped $Ce_{0.8}Sn_{0.2}O_2$ simulated with $Ce_{25}Sn_6Pd_1O_{63}$ supercell (see Figure 9c), the Ce coordination can be approximated to 4 + 4, with mean short and long Ce−O bond lengths equal to 2.24(0.03) and 2.43(0.16) Å. Coordination of Sn can be approximated to 4 + 2 + 2, with the mean distances of 2.04(0.02), 2.38(0.19) and 2.73(0.08) Å respectively. Coordination of Pd is 4 + 3 with the mean bond lengths equal to 2.12(0.09) and 2.72(0.1) Å. The deviation of the mean bonds for the second and third coordination shell is larger than the first coordination shell, indicating the presence of disordered oxygen sublattice in the structure. The local coordination of Ce, Sn, and Pd determined from EXAFS studies match reasonably well with DFT calculations. The short Ce−O, Sn−O, and Pd−O bond lengths corresponding to first coordination shell from our theoretical calculations agree well with those from the EXAFS analysis. The longer bonds obtained from DFT calculations are larger than the bond distances obtained from the EXAFS study.

From H_2/TPR studies we have seen that the presence of partial oxygen vacancies further destabilizes the oxygen sublattice, as a result of which peak reduction temperature decreases from 110 to 45 °C. To see the effect of oxygen vacancy on the bonds distribution, three oxygens were removed from $Ce_{25}Sn_6Pd_1O_{63}$ supercell and the resultant $Ce_{25}Sn_6Pd_1O_{60}$ lattice was optimized. The comparative bonds distribution plots are given in Figure 10. Though a few Sn−O and Pd−O bonds became longer, the overall distribution of the Ce−O and Sn−O bonds has become narrower. The Sn−O bonds get distributed into three distinct regions with the mean bond lengths of

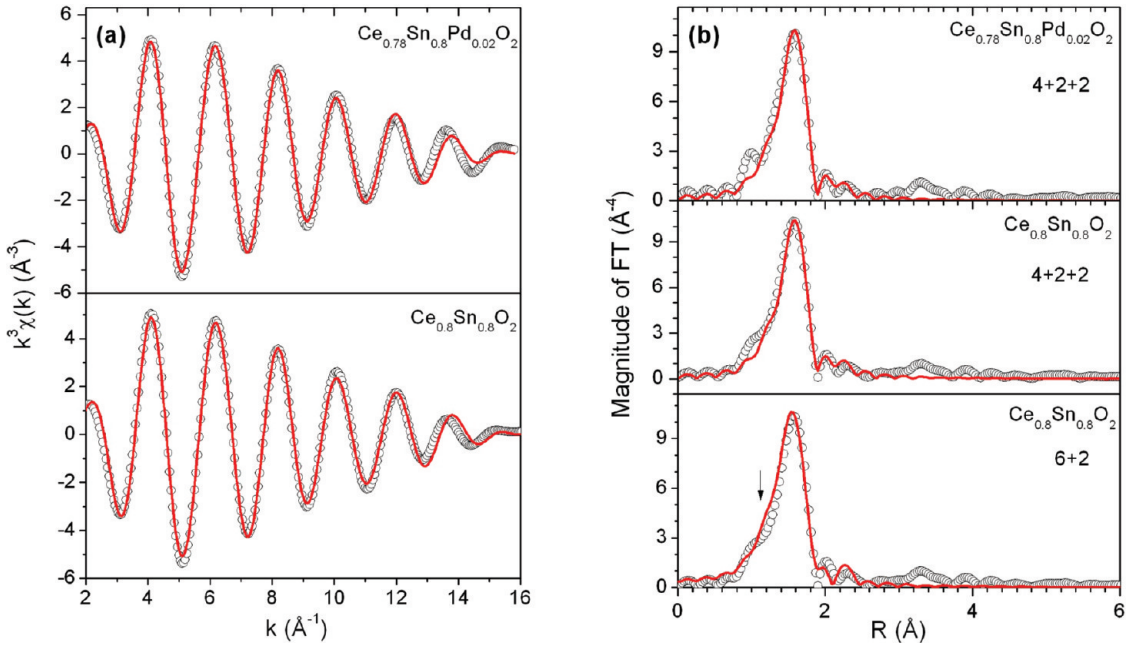

Figure 7. (a) Background-subtracted EXAFS spectra at the Sn *K*-edge of $Ce_{0.8}Sn_{0.8}O_2$ and $Ce_{0.78}Sn_{0.8}Pd_{0.02}O_{1.98}$, and (b) the corresponding FT with the fits for 6 + 2 and 4 + 2 + 2 coordination (solid lines).

2.08(0.02), 2.28(0.06), and 2.51(0.05) Å, respectively. The Sn−O bonds at 2.92 Å are too long and are therefore considered as nonbonding distance. The longer Pd−O and Sn−O bonds created in the oxygen deficient material have oxygen sites that are highly activated, and can be easily removed from the lattice above room temperature as seen from H_2/TPR experiment (Figure 5).

To check the effect of doping higher percentage of Sn in CeO_2 lattice, $Ce_{0.5}Sn_{0.5}O_2$ and $Ce_{0.5}Sn_{0.48}Pd_{0.02}O_{1.98}$ were simulated using $Ce_{16}Sn_{16}O_{64}$ and $Ce_{16}Sn_{15}Pd_1O_{63}$ lattice, respectively. The distributions of bond lengths calculated from the optimized structure (see Figure 11) shows that $Ce_{16}Sn_{16}O_{64}$ system has Ce in 4 + 4 coordination (see Figure 11a) and the mean short and long bonds are 2.26(0.05) and 2.43(0.01) Å, respectively. The Sn−O bonds are clearly grouped over three distinct regions in 4:2:2 ratio, with mean distances of 2.01(0.05), 2.33(0.08), and 2.99(0.12) Å, respectively. Since larger numbers of Sn−O bonds are longer compared to $Ce_{26}Sn_6O_{64}$ system, the OSC of $Ce_{0.5}Sn_{0.5}O_2$ for reduction up to 550 °C is higher compared to $Ce_{0.8}Sn_{0.2}O_2$ (see Table 2). With the introduction of Pd^{2+} ion, the Ce−O and Sn−O bonds exhibit wider distribution (Figure 11b) and the mean Ce−O and Sn−O bond lengths are the same as those in $Ce_{16}Sn_{16}O_{64}$. Pd is essentially in square pyramidal geometry with 4 + 1 coordination and the mean bond lengths are 2.03(0.05) and 2.47 Å, respectively; also Pd−O bonds are longer than those obtained for $Ce_{25}Sn_6Pd_1O_{63}$ system (compare Figure 9c and 11b). This is consistent with the fact that $Ce_{0.5}Sn_{0.48}Pd_{0.02}O_{2-\delta}$ gave H_2/TPR peak at temperature lower than that of $Ce_{0.78}Sn_{0.2}Pd_{0.02}O_{2-\delta}$ (see Figure 3).

To indentify the weakly bonded oxygen in each lattice, bond valence analyses was used taking into consideration the optimized M−O (M = Ce, Sn, Pd) bond lengths. Parameters used in bond valence analysis are given in Table 7. Our estimates of bond valence of Ce and O in CeO_2 are 3.98 and 1.99, which are close to the oxidation state of Ce and O in CeO_2 (Figure 12a). Bond valence distribution of oxygen in $Ce_{26}Sn_6O_{64}$, shown in panel b of Figure 12, clearly indicates that substantial distortion of the oxygen sublattice, leading to distribution of bond valence of oxygen from 1.65 to 2.3 compared to ideal value of 2 in CeO_2. Oxygen with 1 short Sn−O bond and 3 long Ce−O bonds have valency ∼1.7, whereas oxygen with 1 long Sn−O/Ce−O bond and 3 short Ce−O bonds have valency ∼2.3 (see Table 5). Oxygen ions with bond valence less than 2 can be considered to be weakly bonded to the lattice, whereas oxygen with bond valence greater than 2 can be considered to be strongly bonded to the lattice.

With incorporation of Pd in $Ce_{26}Sn_6O_{64}$ (i.e., $Ce_{25}Sn_6Pd_1O_{63}$ lattice), a similar trend in bond length distributions is observed (see Figure 12c). The bond valence of oxygen is more broadly distributed over the region: oxygens with 1 short Sn−O or Pd−O and 3 long Ce−O bonds have the lowest bond valence of about 1.65, whereas oxygen with 1or 2 short Ce−O and other long Ce−O/Sn-O bonds have bond valence of about 2.33. With the introduction of oxygen vacancies, the bond valence distribution shifts toward lower value (panel d), indicating an overall destabilization of the oxygen sub lattice.

For $Ce_{16}Sn_{16}O_{64}$, the bond valence distribution is confined within two prominent regions centered at 1.7 and 2.2 (see Figure 12e). Oxygen with bond valence in the region centered at 1.7 has 2 short Sn−O bonds and 2 long Ce−O bonds, whereas oxygen in the bond valence region centered at 2.2 has mostly coordination number 3, of which one is a short Sn−O bond and two are short Ce−O

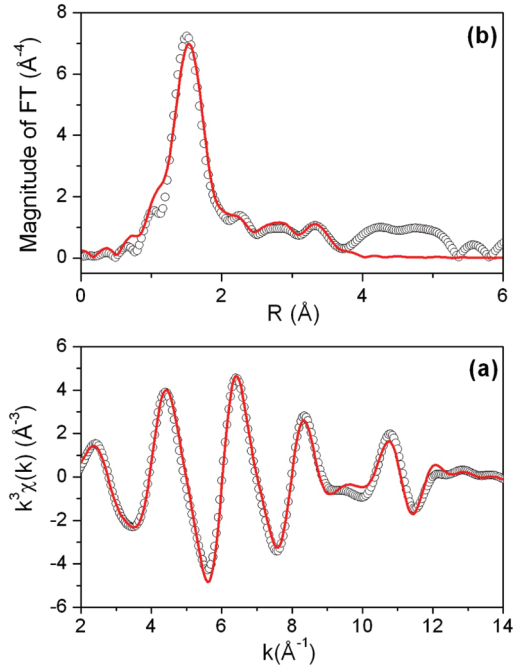

Figure 8. (a) The background subtracted EXAFS spectra at the Pd K-edge of $Ce_{0.8}Sn_{0.8}O_2$ and $Ce_{0.78}Sn_{0.8}Pd_{0.02}O_{1.98}$ and (b) the corresponding FT along with the fits (solid lines).

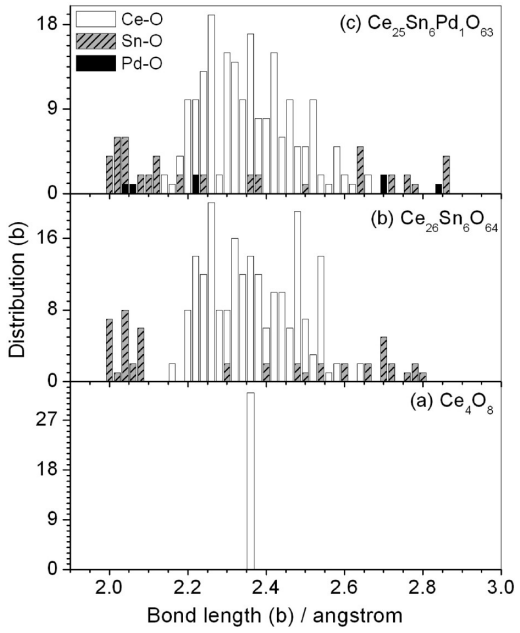

Figure 9. Distribution of M−O bond lengths (M = Ce, Sn, Pd) of (a) Ce_4O_8, (b) $Ce_{26}Sn_6O_{64}$, and (c) $Ce_{25}Sn_6Pd_1O_{63}$.

bonds. The two regions of the oxygen bond valence distribution indicate ordering in the oxygen sublattice. From bond length distribution too, we have observed a clear 4 + 4 coordination of Ce and 4 + 2 + 2 coordination of Sn. With the presence of Pd in $Ce_{16}Sn_{15}Pd_1O_{63}$ lattice, similar to the bond-length distribution, the bond valence becomes more distributed compared to $Ce_{16}Sn_{16}O_{64}$ (panel f). We also observe that a few oxygen are too weakly held by the lattice with bond valence as low as 1.4, leading to some of the oxygen becoming stronger with bond valence more than 2.5. These weakly held lattice oxygen ions are responsible for the low temperature peak at ~90 °C in the H_2/TPR experiment.

Table 5. Typical Ce−O and O−M Bond Length Obtained from Optimized $Ce_{26}Sn_6O_{64}$ Structure

Ce type	Ce−O (Å)	Ce type	Ce−O (Å)	Ce type	Ce−O (Å)
Ce (2)	2.1853	Ce(16)	2.2232	Ce(39)	2.2245
	2.2116		2.2522		2.2589
	2.2118		2.2522		2.2652
	2.2127		2.2553		2.3198
	2.4949		2.4464		2.3931
	2.5268		2.4464		2.4380
	2.5303		2.4929		2.4611
	2.5739		2.4969		2.4651
Ce(50)	2.2091	Ce(62)	2.2550	Ce(75)	2.2829
	2.2091		2.2568		2.3210
	2.2097		2.2624		2.3284
	2.2564		2.3618		2.3328
	2.4294		2.3875		2.3458
	2.5298		2.4132		2.3513
	2.5299		2.4410		2.3667
	2.5448		2.4633		2.4487
O(5)	2.2121(Ce)	O(17)	2.0721(Sn)	O(23)	2.2098(Ce)
	2.2531(Ce)		2.3215(Ce)		2.2321(Ce)
	2.2542(Ce)		2.3691(Ce)		2.2322(Ce)
	2.7102(Sn)		2.6391(Ce)		2.7896(Sn)
O(36)	2.0268(Sn)	O(80)	2.2169(Ce)	O(93)	2.0685(Sn)
	2.4115(Ce)		2.3310(Ce)		2.4012(Ce)
	2.4775(Ce)		2.3315(Ce)		2.4189(Ce)
	2.5215(Ce)		2.5021(Ce)		2.5436(Sn)

Synergistic Electronic Interaction. The reason behind activation of lattice oxygen is, therefore, rationalized on the basis of the fact that dopant Sn embedded in fluorite CeO_2 lattice distorts the oxygen sublattice both around itself and Ce, thus creating longer and shorter bonds. The effect of distortion is more pronounced in $Ce_{0.5}Sn_{0.5}O_2$ system where Ce exhibits 4 + 4 coordination and Sn exhibits 4 + 2 + 2 coordination. Presence of Pd^{2+}, in addition to having usual effect of larger ion being replaced by smaller ion, induces additional distortion in the lattice because of oxide ion vacancy creation for charge compensation. While high oxygen storage/release property is related to inherent structure of the solid solution, sharp H_2-uptake peak at temperature as low as ~110 °C in presence of Pd^{2+} ion is still unanswered. This indicates the crucial role of Pd^{2+} ion in lowering the temperature at which H_2 extracts the lattice oxygen.

In H_2/TPR study, $Ce_{0.8}Sn_{0.2}O_2$ is reduced to oxygen deficient compound given by the reaction:

$$Ce_{0.8}Sn_{0.2}O_2 + 0.29H_2 \rightarrow Ce^{4+}_{0.62}Ce^{3+}_{0.18}Sn^{2+}_{0.2}O_{1.71} + 0.29H_2O \quad (1)$$

This hydrogen intake reaction is very sluggish and starts from 200 to 500 °C, that is, activated oxygen though present in the lattice is not active enough and spans a wide temperature range. This same amount of reduction is achieved in a single reduction at ~110 °C in presence of Pd^{2+} ion, namely, $Ce_{0.78}Sn_{0.2}Pd_{0.02}O_{2-\delta}$ catalyst, and the reaction is given as

$$Ce_{0.78}Sn_{0.2}Pd_{0.02}O_{1.98} + 0.28H_2 \rightarrow Ce^{4+}_{0.66}Ce^{3+}_{0.12}Sn^{2+}_{0.2}Pd^{0}_{0.02}O_{1.70} + 0.28H_2O \quad (2)$$

Table 6. Coordination Number and Mean Bond Lengths from the Optimized Structure

compound	cell used for DFT calculation	coordination shell	C.N.	average bond length (Å)
CeO_2	Ce_4O_8	Ce−O	8	2.34
$Ce_{0.8}Sn_{0.2}O_2$	$Ce_{26}Sn_6O_{64}$	Ce−O	4 + 4	2.26(0.05), 2.45(0.12)
		Sn−O	4 + 2 + 2	2.03(0.03), 2.46(0.15), 2.71(0.06)
$Ce_{0.78}Sn_{0.2}Pd_{0.02}O_{1.98}$	$Ce_{25}Sn_6Pd_1O_{63}$	Ce−O	4 + 4	2.24(0.03), 2.43(0.16)
		Sn−O	4 + 2 + 2	2.04(0.02), 2.38(0.19), 2.73(0.08)
		Pd−O	4 + 3	2.12(0.09), 2.72(0.1)
	$Ce_{25}Sn_6Pd_1O_{60}$ (with oxygen vacancy)	Ce−O	4 + 4	2.23(0.06), 2.4(0.1)
		Sn−O	4 + 2 + 2	2.08(0.02), 2.28(0.06), 2.51(0.05)
		Pd−O	3 + 2	2.17(0.15), 3.24(0.04)
$Ce_{0.5}Sn_{0.5}O_2$	$Ce_{16}Sn_{16}O_{64}$	Ce−O	4 + 4	2.26(0.05), 2.43(0.01)
		Sn−O	4 + 2 + 2	2.01(0.05), 2.33(0.08), 2.99(0.12)
$Ce_{0.5}Sn_{0.48}Pd_{0.02}O_{1.98}$	$Ce_{16}Sn_{15}Pd_1O_{63}$	Ce−O	4 + 4	2.26(0.05), 2.46(0.08)
		Sn−O	4 + 2 + 2	2.01(0.05), 2.36(0.08), 2.98(0.11)
		Pd−O	4 + 1	2.03(0.05), 2.47

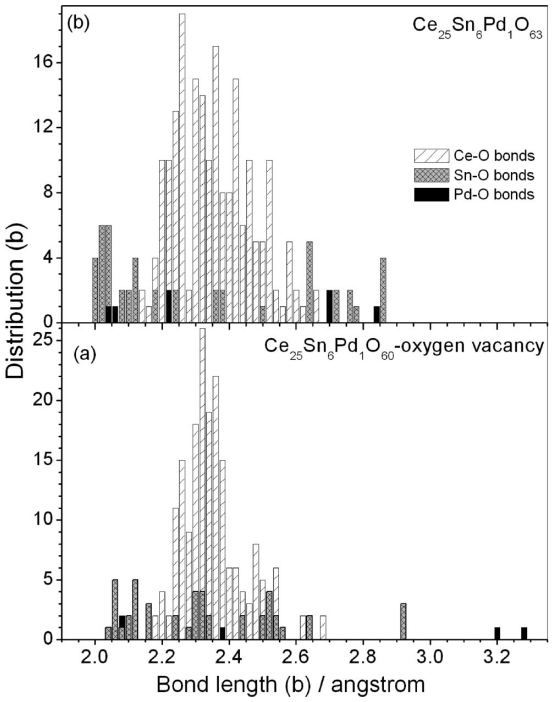

Figure 10. M−O bond length distribution of (a) $Ce_{25}Sn_6Pd_1O_{60}$ (with oxygen vacancy) compared with (b) $Ce_{25}Sn_6Pd_1O_{63}$.

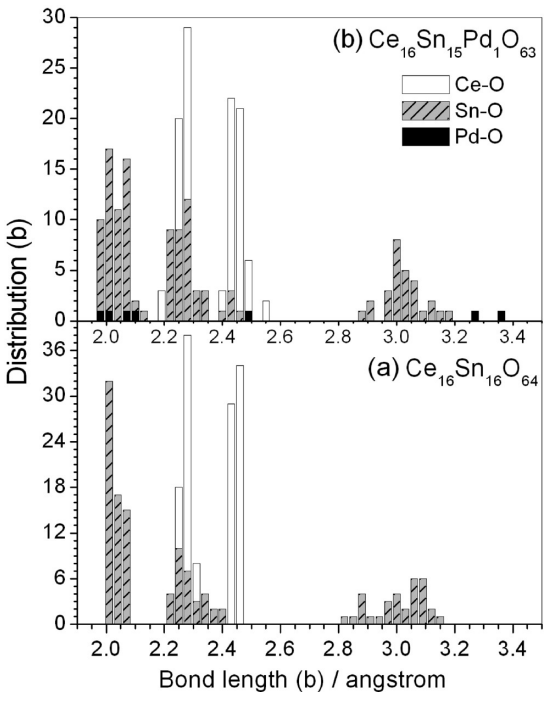

Figure 11. M−O bond length distribution of (a) $Ce_{16}Sn_{16}O_{64}$ and (b) $Ce_{16}Sn_{15}Pd_1O_{63}$.

In an earlier study, we had shown that H_2 chemisorbed on Pd^{2+} exists as protonic $H_2^{\delta+}$ species, leading to high rates of hydrogen dissociation.[41] The dissociated hydrogen in conjunction with the availability of activated lattice oxygen is responsible for the synergistic reduction of Ce^{4+}, Sn^{4+}, and Pd^{2+} ions in $Ce_{0.78}Sn_{0.2}Pd_{0.02}O_{1.98}$ oxide, resulting in sharp reduction peak observed in H_2/TPR study.

Extensive XPS studies of these samples have shown that Ce is in +4 oxidation state, Sn is in +4 state, and Pd is in +2 state.[8] When the sample is reduced in H_2 (H_2/TPR cycle) at 400 °C, all Sn^{4+} reduces to Sn^{2+}, Pd^{2+} to Pd^0 and some of Ce^{4+} reduces to Ce^{3+} state. Oxidation of the reduced sample at 400 °C induces complete oxidation of Sn^{2+}, Pd^0, and Ce^{3+} to their original oxidation states. This led us to believe that some kind of electronic equilibrium is established between the three redox couples, namely Ce^{4+}/Ce^{3+}, Sn^{4+}/Sn^{2+} and Pd^{2+}/Pd^0, which may be responsible for single sharp peak of H_2 consumption. To probe the electronic origin of activated oxygen at lower temperatures, we examined the valence band spectra of Pd-metal, CeO_2, $Ce_{0.98}Pd_{0.02}O_{1.98}$, SnO and SnO_2 (Figure 13). The VB spectrum of CeO_2 (shown in the Figure 13) has occupied density of states only due to O (2p) band starting at ~3 eV from E_F (Fermi level) which is consistent with absence of electrons in Ce^{4+}(4f) level (located ~2 eV from E_F, Fermi level).[42] The difference of the VB spectra of CeO_2 and $Ce_{0.98}Pd_{0.02}O_{1.98}$ shows a

Table 7. Parameters Used for Bond Valence Calculation

type of bond	R_0	fitted parameter
Ce−O	2.117	$B = 0.326$
Pd−O	1.792	$B = 0.37$
Sn−O	1.955	$N = 8.1$

(41) Sharma, S.; Hegde, M. S. *ChemPhysChem* **2009**, *10*, 637.

(42) Sarma, D. D.; Hegde, M. S.; Rao, C. N. R. *J. Chem. Soc., Faraday Trans. 2* **1981**, *77*, 12.

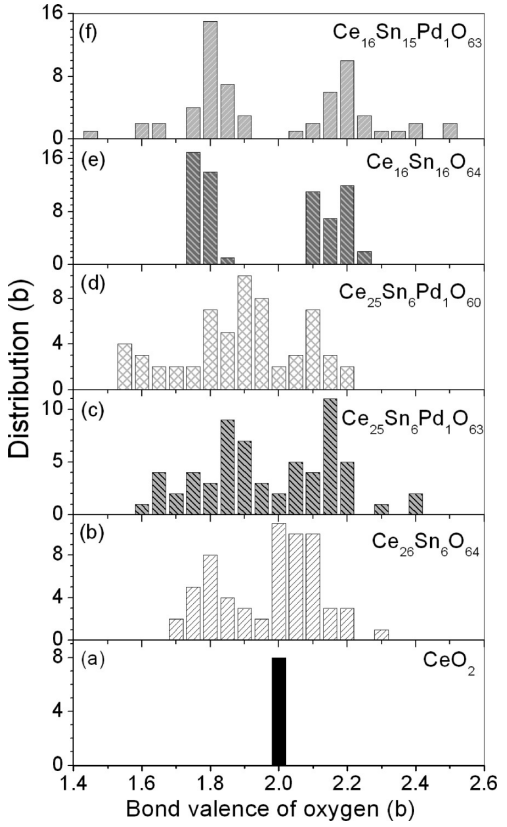

Figure 12. Oxygen bond valence distributions (a) CeO_2, (b) $Ce_{26}Sn_6O_{64}$, (c) $Ce_{25}Sn_6Pd_1O_{63}$, (d) $Ce_{25}Sn_6Pd_1O_{60}$, (e) $Ce_{16}Sn_{16}O_{64}$, and (f) $Ce_{16}Sn_{15}Pd_1O_{63}$.

small density of states at ~3.2 eV from the E_F. This density of states corresponds to $Pd^{2+}(4d^8)$ occupied state which has been magnified 10 times in the y-scale. Similarly, the valence band region of SnO_2 consists of only O(2p) band. VB of SnO has significant electron density, besides O 2p states, because of filled Sn $5s^2$ band. The difference of the VB spectra of SnO and SnO_2 shows the presence of $Sn^{2+}(5s^2)$ band at ~3 eV from Fermi level (E_F). VB of Pd-metal ($4d^85s^2$) has high density of states at the E_F. Thus, to summarize, $Ce^{3+}(4f^1)$ band lies at ~2 eV from Fermi level, $Pd^{2+}(4d^8)$ at ~3.2 eV and $Sn^{2+}(5s^2)$ at ~3 eV.

Reduction of $Ce_{0.8}Sn_{0.2}O_2$ up to 550 °C in H_2 has shown the presence of Sn^{2+} and Ce^{3+} oxidation states,[8] while for $Ce_{0.78}Sn_{0.2}Pd_{0.02}O_{2-\delta}$ same extent of reduction is achieved at 110 °C. The sharp H_2 consumption peak with H_2/Pd ratio 14 implies that reduction temperature of Sn^{4+} and Ce^{4+} is also brought down to the temperature at which Pd^{2+} is reduced to Pd^0 by H_2. VB spectra shows that the reduction of Pd^{2+} to Pd^0 shifts the electron density toward the Fermi level, and therefore it lies above the empty Sn^{4+} ($5s^05p^0$) and Ce^{4+} ($4f^0$) bands in the energy scale. Therefore, transfer of electrons from Pd^0 to Sn^{4+} ($5s^05p^0$) and Ce^{4+} ($4f^0$) is favorable; so the following reduction reaction is established because of Pd^{2+} reduction to Pd^0:

$$Pd^0 + 2Ce^{4+} \rightarrow Pd^{2+} + 2Ce^{3+} \quad (3)$$

$$Pd^0 + Sn^{4+} \rightarrow Pd^{2+} + Sn^{2+} \quad (4)$$

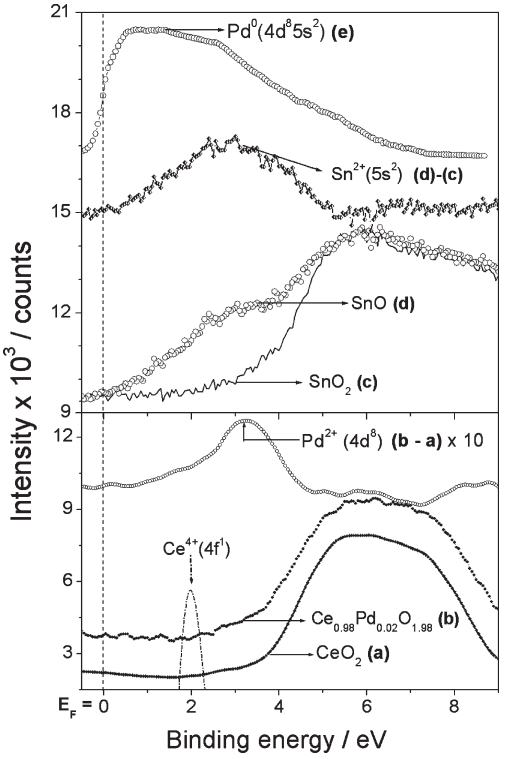

Figure 13. Valence band XPS spectra of (a) CeO_2, (b) $Ce_{0.98}Pd_{0.02}O_{1.98}$, (c) SnO_2, (d) SnO, and (e) Pd-metal. Difference spectra of (a)−(b) represents $Pd^{2+}(4d^8)$ band (magnified 10 times in *y*-scale) and (d)−(c) represents $Sn^{2+}(5s^2)$ band.

To check the validity of the eqs 3 and 4 additional experiments were carried out with Pd metal impregnated CeO_2 and SnO_2. Two atom % Pd impregnated oxide were made into a pellet and were heated at 400 °C under Ar-flow for 4 h. Binding energy peak of Pd($3d_{5/2}$) core level of as-prepared Pd-impregnated CeO_2, shown in Figure 14a, at 335.2 eV is the result of Pd^0 state.[43] For the sample heated in Ar at 400 °C in absence of oxygen, Pd($3d_{5/2}$) core level peak shifts to higher binding energy at 337.2 eV assigned to Pd^{2+} oxidation state[43] though trace amount of Pd^0 state is present in the sample (Figure 14b). This reaction is favorable because the electron transfer from higher Pd^0 band near Fermi level to empty Ce^{4+}(4f) lying below E_F is facilitated. Similar results were observed for Pd impregnated SnO_2 samples. In this case, Pd is completely oxidized to Pd^{2+} state when the sample was heated under Ar-flow (Figure 14c,d). Hence the redox process is given as

$$xPd^0 + (1-x)CeO_2 \rightarrow Ce_{1-x}Pd_xO_{2-2x} \quad (5)$$

$$xPd^0 + (1-x)SnO_2 \rightarrow Sn_{1-x}Pd_xO_{2-2x} \quad (6)$$

These two solid state reaction are equivalent to eq 3 and 4 corroborating the fact that electronic interaction between the cations in the solid solution becomes active when Pd^{2+} is reduced to Pd^0 state. Hence, simultaneous reduction of Ce^{4+} and Sn^{4+}, along with the Pd^{2+} ion with

(43) Briggs, D.; Seah, M. P. *Practical Surface Analysis*; John Wiley & Sons Ltd.: New York, 1983

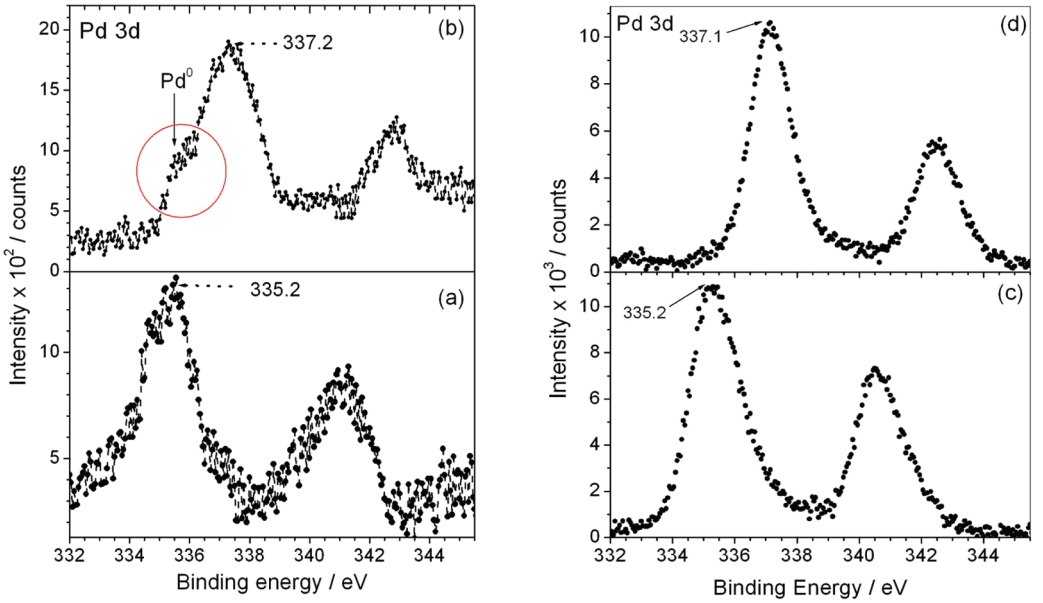

Figure 14. Pd 3d core level spectra of (a) as-prepared 2 atom % Pd-impregnated CeO_2, (b) 2 atom % Pd-impregnated CeO_2 sample heated in Ar at 400 °C for 4 h, (c) as-prepared 2 atom % Pd impregnated SnO_2, and (d) 2 atom % Pd impregnated SnO_2 sample heated in Ar at 400 °C for 4 h.

H_2 is responsible for sharp single step reduction of $Ce_{0.78}Sn_{0.2}Pd_{0.02}O_{2-\delta}$.

4. Conclusion

Combined EXAFS and first-principles theoretical analysis of the solid solutions $Ce_{1-x}Sn_xO_2$ and $Ce_{1-x-y}Sn_xPd_yO_{2-\delta}$ have shown that Ce is in 4 + 4 coordination, Sn in 4 + 2 + 2 coordination, and Pd in 4 + 3 coordination. With increasing Sn concentration, the distribution of the coordination number becomes more pronounced. Both $Ce_{0.5}Sn_{0.5}O_2$ and its Pd-substituted analogue have Sn−O and Pd−O bonds longer compared to $Ce_{0.8}Sn_{0.2}O_2$ and $Ce_{0.78}Sn_{0.2}Pd_{0.02}O_{2-\delta}$. Bond valence analyses reveals that oxygens with longer M−O (M = Ce, Sn, Pd) are weaker and therefore activated. Simultaneous reduction of the Ce^{4+} and Sn^{4+} ions by Pd^0 is the synergistic interaction leading to high oxygen storage capacity at low temperature.

Acknowledgment. We are grateful to Mr. Anil Kumar (JNCASR) for many helpful discussions and inputs regarding theoretical calculations. The authors thank the central computing facility at JNCASR for use of computational resources, and UVW acknowledges the funding from the DAE-SRC project grant. The authors gratefully acknowledge financial support from the Department of Science and Technology (DST), Government of India.